Northumbria Research Link

Northumbria University NEWCASTLE

UniversityLibrary

How oxygen exposure improves the back contact and performance of antimony selenide solar cells

Nicole Fleck,[‡] Oliver S. Hutter,[‡] Laurie J. Phillips,[‡*] Huw Shiel, Theodore D.C. Hobson, Vin R. Dhanak, Tim D. Veal, Frank Jäckel, Ken Durose and Jonathan D. Major

Abstract

The improvement of antimony selenide solar cells by short-term air exposure is explained using complementary cell and material studies. We demonstrate that exposure to air yields a relative efficiency improvement of n-type Sb_2Se_3 solar cells of *ca.* 10% by oxidation of the back surface and a reduction in the back contact barrier height (measured by *J-V-T*) from 320 meV to 280 meV. XPS measurements of the back surface reveal that during 5 days in air, Sb_2O_3 content at the sample surface increased by 27% leaving a more Se-rich Sb_2Se_3 film along with a 4% increase in elemental Se. Conversely, exposure to 5 days of vacuum resulted in a loss of Se from the Sb_2Se_3 film, which increased the back contact barrier height to 370 meV. Inclusion of a thermally evaporated thin film of Sb_2O_3 and Se at the back of the Sb_2Se_3 absorber achieved a peak solar cell efficiency of 5.87%. These results demonstrate the importance of a Se-rich back surface for high efficiency devices and the positive effects of an ultra-thin antimony oxide layer. This study reveals a possible role of back contact etching in exposing a beneficial back surface and provides a route to increasing device efficiency.

Introduction

Antimony selenide (Sb_2Se_3) is a relatively new photovoltaic absorber material that has seen a rapid efficiency rise in recent years (from 2.1% to 9.2% since 2014). [1, 2] However, while these increases have been impressive, there is still a gap in the fundamental understanding of its material properties. [3] The interest in Sb_2Se_3 stems from it being a binary, single phase compound that is abundant, has relatively low-toxicity, a near-ideal band gap, and a high absorption coefficient (>10^5 cm^{-1} in the visible region). In addition, it forms 1D-nanoribbon structures that, while presenting challenges due to anisotropic charge transport, offer significant opportunities if the orientation can be controlled with the ribbons orientated perpendicular to the substrate. Within suitably oriented Sb_2Se_3, self-healing grain boundaries have a reduced density of dangling bonds that result in fewer defect states within the band gap. [4] These would act as recombination centres and are usually a major limitation in poly-crystalline thin-film absorbers. Recently, Raman spectroscopy has been shown to allow determination of the preferred orientation for Sb_2Se_3 thin films. [5]

It is common in the study of hybrid organo-halide perovskite solar cells, which can exhibit high power conversion efficiency, to analyse the short-term evolution of efficiency due to their notorious stability issues. [6] Device stability is an important consideration for any emerging technology and most suffer some form of degradation over various timescales. [7] However, for relatively stable solar cells, little attention is paid to changes that occur immediately following cell fabrication, which is important for initial efficiency characterisation and a key indicator of material properties.

In the superstrate architecture for a thin-film solar cell, light enters through the transparent substrate and therefore the back contact (i.e. at the dark side) is exposed and susceptible to being influenced by the air unless it is encapsulated. The rear surface of Sb_2Se_3 determines the quality of the back contact in superstrate devices and is therefore crucial in achieving Ohmic behaviour and low series resistance contacts. There have been numerous etch processes proposed to improve the back-surface, for example CS_2 and $(NH_4)_2S$ chemical treatments, [8, 9] with the proposed benefit generally derived from the removal of antimony oxide. Addition of Se to the back contact has also been suggested as a method of cell improvement. [10, 11]

In this work, we examine the natural aging of superstrate n-type [3] Sb_2Se_3-based cells under atmospheric conditions. During multiple Sb_2Se_3-based device studies, a consistent change in efficiency was observed with repeated measurements over time for samples stored in air. In contrast to many absorbers, an efficiency boost was noted during the first few days after fabrication. This has been observed in the literature previously, [12] but has not been commented on or explored. The improvements are contrasted to cells stored under vacuum. The changes in performance and material properties at the back surface were studied using current density-voltage measurements under illumination (*J-V*) and in the dark at different temperatures (*J-V-T*), as well as x-ray photoelectron spectroscopy (XPS). We examine both the changes occurring at the atomic level and their influence on cell behaviour. Through this combined approach, we show that a small amount of surface oxidation leaves a more selenium-rich

Sb_2Se_3 at the rear surface which reduces the back contact barrier height, increases the fill-factor, and enhances the cell efficiency. Conversely, vacuum exposure increases the back contact barrier height via removal of selenium from the Sb_2Se_3 surface.

Methods

Samples were fabricated for both cell-making and material analysis according to previously published methods, with cells using the $FTO/TiO_2/Sb_2Se_3/Au$ architecture. [13, 14] Different analysis methods such as *J-V, J-V-T* and XPS were performed on the same sample set to minimise sample-to-sample variability. The complete cell structure was used each time apart from for XPS analysis, for which the gold back contact was omitted. An organic hole transport material (HTM) has been used previously to improve cell consistency and efficiency, [13] but was not included in this study to simplify the analysis and avoid confounding factors.

FTO coated glass (TEC10 NSG Ltd.) was ultrasonically cleaned using deionised-water, and isopropanol, then treated in a UV-ozone reactor for 10 minutes. A compact layer of TiO_2 as an electron transport material (ETM) was deposited in a nitrogen filled glove-box using a two-step spin-coating process from a 0.15M and then 0.3M titanium-isopropoxide (Sigma Aldrich, 97%) solution in anhydrous ethanol. [15] Each solution was deposited at 3000 rpm for 30 s, then dried at 120 °C for 10 minutes on a hot-plate. The fully coated sample was then annealed in air at 500 °C for 30 minutes. The Sb_2Se_3 absorber was deposited using a two-step close-spaced sublimation (CSS) process that is detailed elsewhere. [13] In brief, a seed-layer was deposited at a source temperature of 360 °C under vacuum, followed by a growth stage at 460 °C under 13 mbar nitrogen. Finally, the Sb_2Se_3 deposition was halted by a rapid increase in nitrogen pressure to 460 mbar and the layer was cooled to room temperature. 50 nm of gold was then deposited onto a room temperature substrate by thermal evaporation through a shadow-mask to define cells with an area of 0.1 cm^2.

Analysis commenced immediately after fabrication (i.e. time = 0 hr) and was repeated at intervals thereafter during exposure to various conditions. Cells were aged in air by simply leaving them in the lab ambient (room temperature, dark, 1 atm air). Vacuum aging was performed by leaving the cells in a vacuum chamber (room temperature, dark, *J-V-T*: 10^{-4} mbar, XPS: 10^{-10} mbar). Measurements were taken at specified intervals to determine the change in device performance over time.

J-V measurements were performed using a TS Space Systems UniSim 100 AAA-rated solar simulator. Cells were measured with a voltage sweep from -1 V to +1 V at a rate of 0.25 V/s without any conditioning prior to measurement. *J-V-T* measurements used a Janis cryostat to measure the dark *J-V* curves of cells from -1 V to +1 V at each temperature between 200 K and 350 K in 10 K increments. The back contact barrier height (φ_{BCB}) was extracted using the Bätzner method [16] using a fit to the series resistance of the cell as a function of temperature. XPS experiments were performed in an ultrahigh vacuum (UHV) surface science chamber operating at a base pressure of 1 × 10^{-10} mbar. Core-level spectra were measured

in normal emission geometry using a Mg K_α (1253.6 eV) x-ray source operating at 144 W and a hemispherical PSP Vacuum Technology electron energy analyser. XPS spectra were fitted using a Gaussian/Lorentzian product function to approximate a Voigt function [17] after Shirley background [18] fitting with a binding energy determination precision of ± 0.1 eV. The secondary electron cut-off (SEC) was measured with the x-ray source operating at 9 W and an applied bias of 10 V between the sample and analyser. Raman spectroscopy was carried out using a Renishaw inVia microscope in backscattering geometry with a 633 nm laser. The power was kept below 0.05 mW at the sample to prevent laser damage to the surface. [5]

Results and discussion

In order to investigate the aging process of the Sb_2Se_3 cells, *J-V* measurements were taken at intervals after exposure to ambient air, allowing an assessment of the performance change induced. Fig. 1 shows *J-V* curves taken from the same cell at 0, 23, 50 and 98 hours after fabrication and storage in air, with the parameters of the cells summarized in Table 1. The most obvious change to the curves over time is the reduction in the limitation to the forward current (known as the 'roll-over' [19, 20]) that occurs at high forward bias in the light J-V curves. The diode due to the back contact, which acts in opposition to the main junction diode, limits majority-carrier injection at bias greater than V_{oc}. [21] The reduction in this roll-over over with time suggests a reduction in the back contact barrier height induced by the air exposure. Fig. 1 also shows some qualitative differences between the development of the J-V curve shapes when comparing the evolution of the light and dark curves during air exposure. The light J-V curves undergo a rapid transition from having very significant to very reduced roll-over (0 – 23 hrs), to the longer-term air exposed samples showing J-V curves that converge (50 and 98 hrs). However, the dark J-V curves show less pronounced roll-over and initially change shape more slowly with air exposure (0 and 23 hrs overlap) and only begin to diverge with longer exposure (50 – 98 hrs). It is
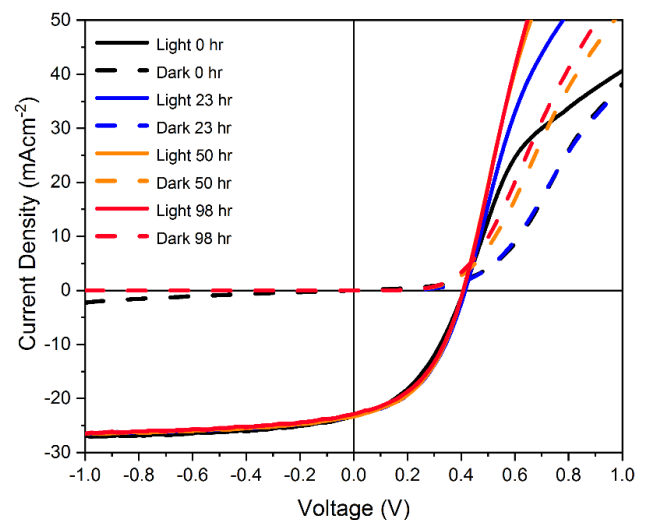

Figure 1: Light and dark current-voltage plots of the same cell after 0, 23, 50, and 98 hours exposure to ambient air, showing the reduction in roll-over with time.

likely that these differences are due to a photo-response in the material, but the curves alone cannot be used to determine whether they are due to photoconductivity or photo-excitation of traps for example. No change in optical absorption was observed, as shown in Fig. S1.

Table 1: Efficiency (η), V_{oc}, J_{sc} and FF of the cell in Fig. 1, measured immediately after fabrication, and after exposure to air for 23, 50, and 98 hours.

	0 hrs	23 hrs	50 hrs	98 hrs
η (%)	3.90	4.31	4.28	4.16
V_{oc} (V)	0.410	0.415	0.407	0.408
J_{sc} (mA cm^{-2})	23.3	23.2	23.3	22.9
FF (%)	41.8	44.2	45.9	45.5

The curves shown in Fig. 1 are from a single cell, but it is representative of the general trend observed from the data set, as can be seen in Fig. 2 and S2. The efficiency increase over the initial 23 hr period is driven by increases in the fill factor, while there is little change in the J_{sc} and V_{oc}. In contrast, samples exposed for 5 days to vacuum, show the opposite trend (Fig. S3). For these, the efficiency has decreased slightly driven by an unchanged V_{oc} and FF, combined with the J_{sc} showing similar reduction after 5 days compared to the samples exposed to air. The lack of performance improvement under vacuum indicates that air exposure, rather than time itself, causes the device improvements.
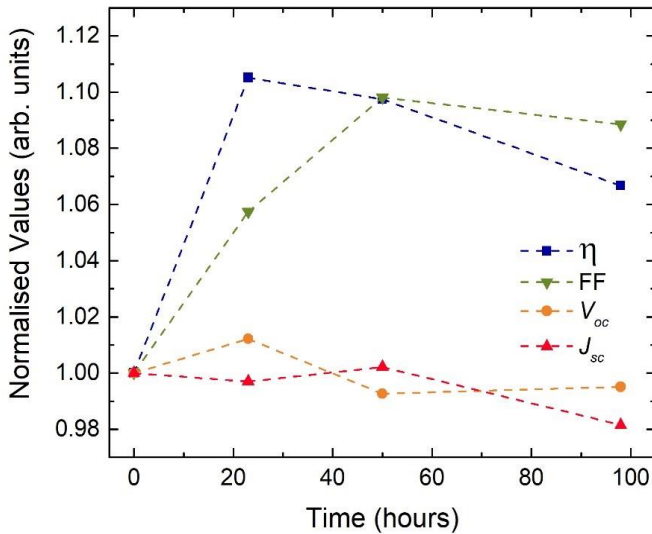
Figure 2: Variation in average device performance parameters on exposure to air for different lengths of time, normalised to their initial value, (n=22 cells). Lines are included as a guide to the eye.

To investigate possible causes of the performance variation, temperature dependent *J-V* measurements (*J-V-T*) were carried out to determine changes in the back contact barrier height in both air and under vacuum. For this, a batch of cells was divided into two sets. The first set was measured immediately after fabrication, then left under vacuum for 5 days and re-measured. The second was exposed to the ambient air for 5 days and then measured. The barrier heights extracted using the Bätzner method [16] are shown in Fig. 3, with representative fits for
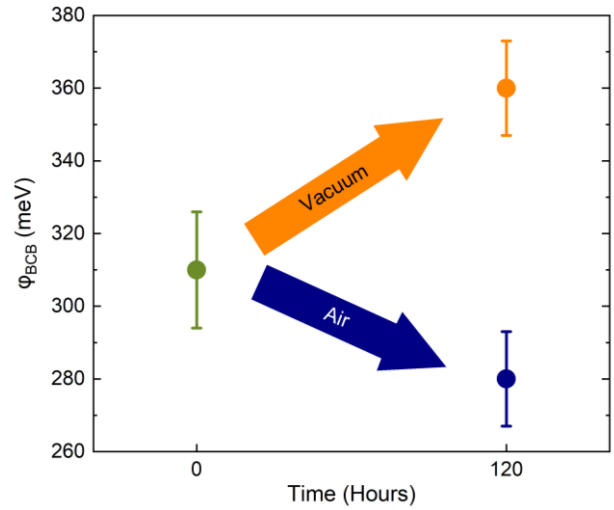

Figure 3: Back contact barrier height for cells, showing the average of 3 cells at 0 hours (i.e. as deposited) and after 120 hours in either air or vacuum. Error bars represent the standard deviation of the measurements.

each sample set showing good quality fits to the data shown in Fig. S4. The change is distinct, with the 5 days in air reducing the barrier by 40 meV. Conversely, the barrier in the sample exposed to 5 days in vacuum increases by approximately the same amount: 50 meV. This suggests that several different processes are occurring at the back-surface of the cells.

One obvious candidate for the change observed in the *J-V* parameters of these cells would be oxidation of the Sb_2Se_3 film to Sb_2O_3 at the back surface. Formation of an oxide could result in the observed change in barrier height. Initially, grazing incidence x-ray diffraction (XRD) and Raman spectroscopy were carried out on a film following 5 days air exposure, as shown in Fig. S5 and S6. All peaks observed were indexed to Sb_2Se_3 [5, 13, 14] demonstrating that either no oxide was present at the surface or that the presence of an oxide, or any other chemical change at the surface, cannot be detected by either of these techniques. The latter was deemed more likely, as some oxide would be anticipated, and was thought to indicate that any chemical changes either formed an amorphous layer or were highly localised at the surface despite the significant effect on device performance. The more surface sensitive technique of XPS was therefore applied to detect any amorphous or crystalline surface layer.

The samples for XPS were taken from the same set as those used for *J-V* measurements, although they did not include the gold back contact. Gold is a relatively porous metal and would not be expected to present a good barrier to the various environmental exposures used in this study. [22, 23] Whilst we recognise that samples used for XPS may experience increased exposure effects without the gold electrode, the change is likely to be minimal and represents the most directly comparable sample which can be measured. All XPS measurements were performed under UHV, and the transfer from Sb_2Se_3 deposition to measurement was undertaken as quickly as possible to minimise the time in air. One sample was measured freshly after fabrication, then kept under vacuum for 5 days and the
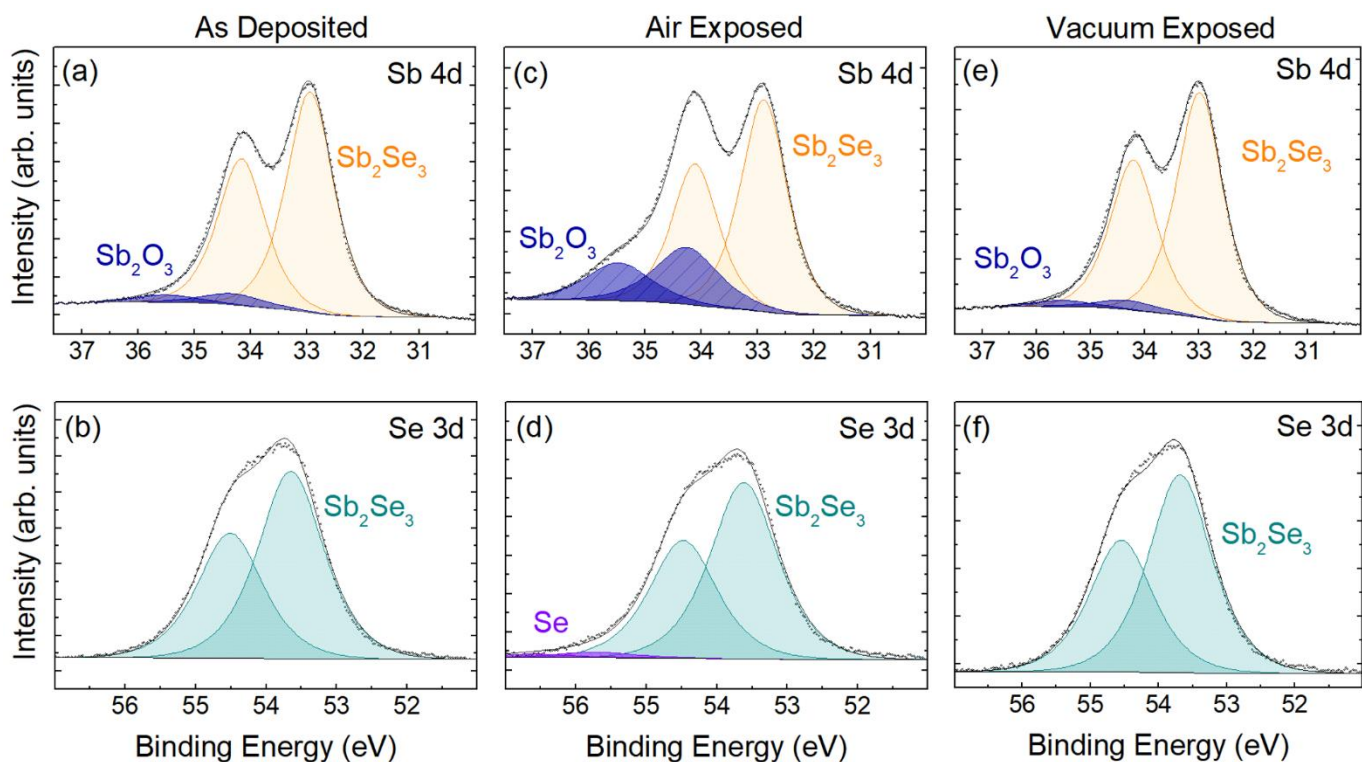
Figure 4: XPS core level (Sb 4d and Se 3d) regions of the freshly prepared (a, b), 5-day air exposed (c, d) and 5-day UHV exposed (e, f) samples.

measurements repeated. A second identical sample was exposed to air for 5 days before measurement.

The peak areas of the fitted XPS spectra were used to quantify differences in the samples. The Sb 4d spectra for example (Fig. 4a, 4c, 4e) show peaks corresponding to Sb in Sb_2Se_3 and Sb in Sb_2O_3. The oxide peaks are assigned to Sb_2O_3 rather than other antimony oxides, such as Sb_2O_5, based on their peak position as discussed in depth by Shiel et al. [8] The percentage of antimony oxide in the spectrum was calculated by dividing the Sb_2O_3 peak area in the Sb 4d spectrum by the total area under the Sb 4d line shape and multiplying this by 100. The same approach was used to determine the percentage of elemental Se in the Se spectra. Spectra from two orbitals of both Sb and Se were fitted and peak areas analysed (Sb 3d, Sb 4d, Se 3d and Se 3p). Electrons originating from different orbitals have different escape depths from within the sample. Those with a low binding energy (high kinetic energy) can escape from greater depths of the sample than electrons with a high binding energy (low kinetic energy). The escape depths of the electrons emitted from different orbitals of Sb_2Se_3 and Sb_2O_3 are summarised in Table S1. This demonstrates that Sb 4d spectra include electrons from deeper inside a Sb_2Se_3 sample (10.2 nm escape depth) than Sb 3d spectra (6.9 nm). Similarly, the Se 3p spectra are more surface sensitive (9.3 nm) than the Se 3d spectra (10.2 nm). Table S1 shows the same trend for a sample of Sb_2O_3 and using this depth profile, the change between surface and sub-surface can be determined by analysis of elemental orbitals at different binding energies. While the signal in all XPS spectra is dominated by the surface of the sample, surface localised changes show more prominently in spectra that are more surface sensitive. The term "sub-surface"

is used here instead of "bulk" due to the extremely small sampling depth of XPS (on the order of nm).

The ratio of peak areas originating from different elements can give information on their relative concentration in the sample. However, the probability of electron ejection from a core level varies from element to element and orbital to orbital as well as the collection efficiency of the detector varying for different electron energies. Atomic photoionization cross sections are known for each orbital given the XPS system setup. [24] In this study, the cross sections are applied to all the peak area calculations however the analyser transmission function (ATF) is not known. The ATF for the Sb 4d and Se 3d spectra will be almost the same, as they are very similar in energy. In calculating the ratios of these sub-surface related peaks the ATF will cancel and thus the absolute value of these ratios is significant. For the surface ratio the ATF will not be the same and therefore only the percentage change in ratio, which is independent of ATF, is discussed. The absolute values remain approximate. The Se to Sb peak area ratio is discussed and the total ratio at the surface and subsurface is calculated (including elemental Se and Sb_2O_3 peak areas) as well as the ratio of the peaks assigned only to Sb_2Se_3. An increase in the latter Se/Sb ratio indicates the loss of Sb bonded to Se, leaving a more Se rich Sb_2Se_3 film while a decrease in the ratio indicates a loss of Se from the Sb_2Se_3 leaving a more Sb rich Sb_2Se_3 layer.

Fig. 4 shows the Sb 4d and Se 3d core level regions of the Sb_2Se_3 surface for the as-deposited, 5-day air exposed and 5-day vacuum exposed samples. The as-deposited samples are composed mainly of Sb_2Se_3 with a small contribution from Sb_2O_3 [8] as seen in Fig. 4a and 4b. After a 5-day exposure to air the Sb_2O_3 content in the sample increased from 6% of the Sb 4d
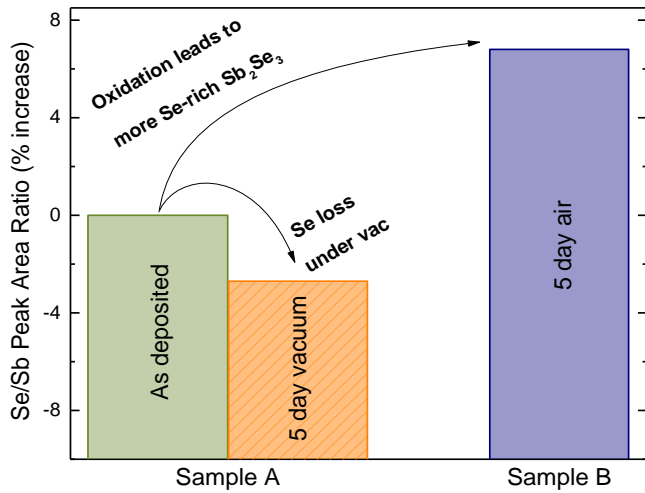
Figure 5: Percentage increase in peak area ratio of Se 3p to Sb 3d Sb_2Se_3 peaks compared to a freshly deposited film. The ratio of "Se bonded to Sb" and "Sb bonded to Se" peak areas were compared to show the loss of selenium under vacuum conditions. The air exposed sample shows a significant increase in Se concentration in comparison to the fresh sample as the Sb reacts with air to form an Sb oxide, leaving a more Se-rich Sb_2Se_3 layer.

spectra to 27% (Table S2). The oxide growth represents the most significant change as evidenced by the clear growth of this peak in Fig. 4c and is likely to play a major role in the device performance improvement in air. However, some additional minor changes were also noted. Table S2 shows the percentage contribution of certain elements in the sample to the total peak area in the spectra.

The Sb 4d spectra were used above to calculate the increase of Sb_2O_3 in the sample. Due to their lower kinetic energy, photoelectrons from Sb 3d orbitals have a lower inelastic mean free path (IMFP) and so correspond to a lower probing depth. If the Sb 3d region is used instead of Sb 4d, the proportion of the Sb 3d region composed of the Sb_2O_3 components increases upon air exposure from 7% to 34% of the total Sb 3d signal (Table S2) indicating the oxide is predominantly formed at the sample surface. The lack of elemental Sb in the samples suggests that the Sb for the oxide growth shown in Fig. 4c stems entirely from breaking bonds in the Sb_2Se_3 and is discussed further below. In Fig. 4 the vacuum exposed sample spectra closely resemble the spectra of freshly deposited samples, indicating that no major chemical changes occur in the sample with time alone. The oxide formation is suppressed under vacuum conditions, however analysis of the ratios of Se to Sb resulted in some interesting findings.

Fig. 5 shows the changes in the ratio of Se to Sb in Sb_2Se_3 (not including oxide peaks or elemental contaminants) for two different samples. Sample A was measured shortly after deposition, left under UHV for 5 days and remeasured while sample B was measured after a 5-day exposure to air. Analysis of the peak area ratios highlights the loss of Se from the Sb_2Se_3 (-3%, see Table S3) under vacuum conditions. Under vacuum, the Sb-Se bond is broken and some Se is removed from the sample leaving a more Se-poor Sb_2Se_3 film. This is expected to be the cause for the decrease in device performance and

increase in the back contact barrier height discussed earlier, for the samples stored under vacuum.

The main change to the sample under atmospheric conditions is the growth of an Sb oxide, leaving a more Se-rich Sb_2Se_3 film and some elemental Se. The oxide is expected to form a thin layer located on the sample surface, further evidenced by the sharp decrease of total Se to total Sb ratio for the air exposed samples (-21% at the surface). The surface ratio of Se to Sb in Sb_2Se_3 increased by almost 7% with air exposure supporting the idea that Sb-Se bonds are broken to form Sb-O bonds, leaving a more Se rich Sb_2Se_3 film and some elemental Se on the surface (4% increase) as shown in Table S3. It is important to note that all XPS measurements were acquired at UHV and thus the ratio of "Se bonded to Sb" to "Sb bonded to Se" may be underestimated for the freshly deposited and air exposed samples. All Se to Sb ratios tabulated in Table S3 show Se-poor Sb_2Se_3, which may be attributed to the initial sample composition, the effects of analysis under vacuum or a combination of both.

The SEC of freshly deposited and air exposed Sb_2Se_3 was measured using XPS to ascertain the work function (WF) of the samples. Fig. 6 shows the SEC spectra and corresponding WF values. The WF of the samples decreases from 4.9 eV to 4.3 eV in air. The shoulder on the freshly prepared sample is thought to be a contribution from a patchy Sb oxide while the main SEC stems from clean Sb_2Se_3. Inhomogeneous sample surfaces are known to display similar SEC spectra. [25] Air exposure encourages further oxide growth leaving the surface coated in a very thin layer of Sb_2O_3 on the order of 1 nm, otherwise the oxide signal would dominate the XPS spectra. This is consistent with the core-level analysis suggesting that air exposure forms a thin layer of Sb oxide on the surface which may act as a protective layer. SEC spectra for vacuum exposed, air-vacuum exposed and vacuum-air exposed samples further corroborate the origin of the spectra and are discussed in Fig. S7 and Section I of the SI. WF measurements were combined with valence band
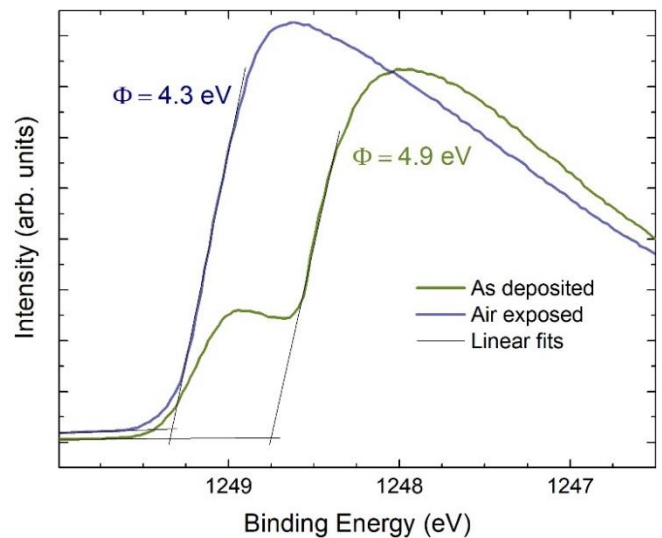
Figure 6: SEC of as deposited and air exposed samples showing the increase in work function of the surface due to oxide and elemental selenium formation. The x-axis has been corrected to account for the 10 V bias applied during measurement.
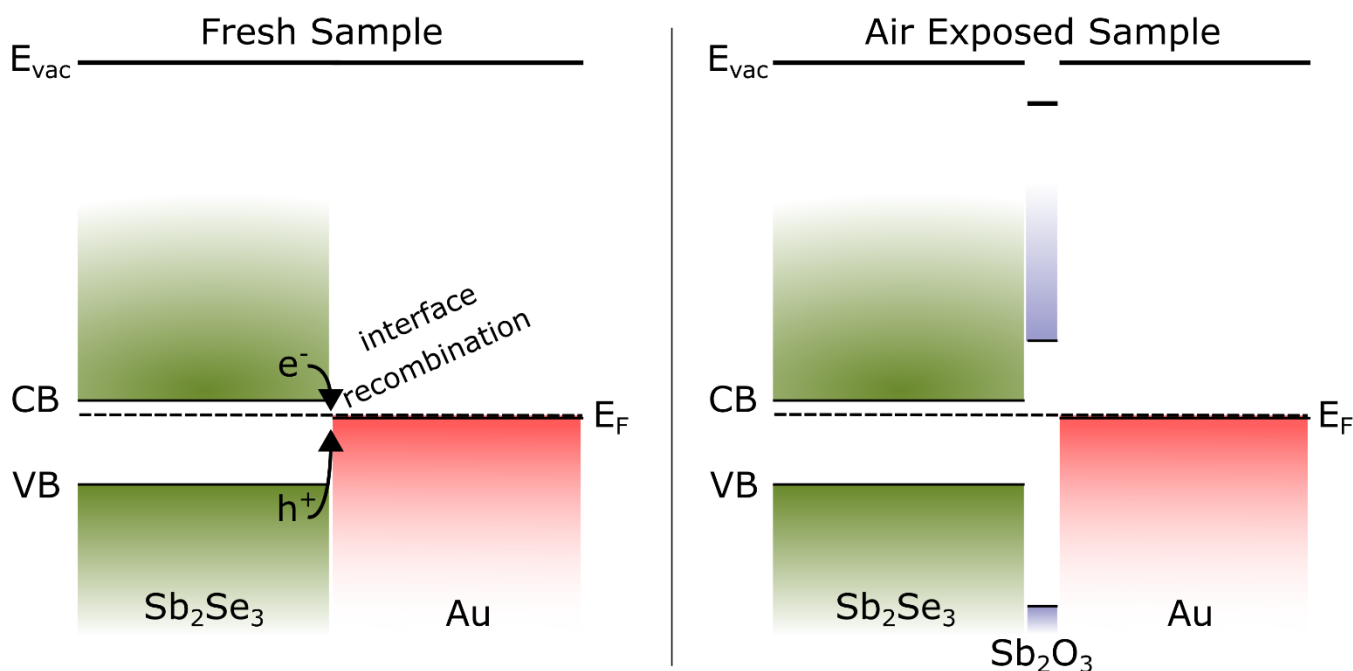
**Figure 7**: Band alignment schematic of fresh and air exposed samples showing the ultra-thin surface layer of Sb_2O_3 formed.

positions (SI Section II) in drawing a band diagram of the junction between the Sb_2Se_3 absorber layer and the gold contact. The band diagram schematic is shown in Fig. 7, with the Sb_2Se_3 depicted as n-type as previously reported. [3] The band offsets are informed by the XPS data discussed above and further measurements discussed in Section II of the SI. During device operation, holes are swept to the back contact and extracted by the gold. The band diagram shows the fresh Sb_2Se_3 layer as well as the conduction band position of a Sb_2O_3 interface layer in contact with the gold. The gold WF was found to equal the Fermi level energy relative to the vacuum level of the freshly prepared sample and thus no charge transfer occurs between the two on contacting. The interface alignment implies that recombination may occur in the freshly deposited samples due to the small (0.22 eV) energy difference between the Fermi level of gold and the conduction band (CB) of Sb_2Se_3. Improvement of device performance by deposition of an additional layer to suppress recombination of charge carriers between Sb_2Se_3 and a gold contact has been reported previously. [26] The ultra-thin surface layer acts as a barrier through which photogenerated holes tunnel, reducing recombination at the back contact. Simultaneously, the oxide surface layer may passivate the interface between the Sb_2Se_3 and Au layers and thereby reduce recombination sites. The diagram suggests that while a thin layer of oxide on the surface may be beneficial, a thicker layer would negatively impact device performance due to its insulating properties increasing the device series resistance.

To confirm that the changes at the sample surface cause the observed performance increase, different attempts were made to controllably reconstruct the changes seen with air exposure. Inducing the formation of a "native" Sb_2O_3 layer by heating in air, as well as depositing a thin layer of Sb_2O_3 and/or a layer of

Se were tested. XPS analysis had already confirmed that surface changes on the order of nm cause the increase in device performance, therefore layers of this scale were targeted.

Freshly prepared Sb_2Se_3 samples were annealed in a box furnace at 300 °C for 5 mins. The device results were extremely poor due to a large device series resistance (Fig. S10), likely the result of the oxide layer being too thick. In addition, the Se within the Sb_2Se_3 layer is known to be volatile from the XPS measurements in this work and therefore it may have been removed during heating, unintentionally causing similar effects to vacuum conditions and contributed to the drop in device performance. Even though it was clearly detrimental to performance, the effect of heating for 5 mins was too subtle to be analysed with Raman spectroscopy. However, a forced oxidation at 300 °C for 15 mins formed a thicker layer, as shown in Fig. S6. The spectrum shows the known major modes of Sb_2Se_3 and those of Sb_2O_3 including the less intense modes at higher wavenumbers. The oxide formed on the surface was found to be α-Sb_2O_3 (senarmonite) which is the most common Sb oxide formed. [26] Both α-Sb_2O_3 and an allotrope of Se (α-monoclinic) display a major Raman peak at ~255 cm^{-1}. [28, 29, 30] While some small amounts of elemental Se may also be present, no secondary peaks were found and the more volatile Se is expected to have evaporated.

The effects of thermal evaporation of thin layers of Sb_2O_3, Se or both onto the surface of the Sb_2Se_3 were compared to establish the origin of the device performance increase. Fig. 8 shows that the improvement of device performance achieved through air exposure can be achieved through thermal evaporation of thin layers of Sb_2O_3 and/or Se. A 2 nm thick layer was deposited onto fresh Sb_2Se_3 and the effects on device performance analysed. Thick evaporated layers were deposited on separate Sb_2Se_3 substrates and Raman spectra confirmed
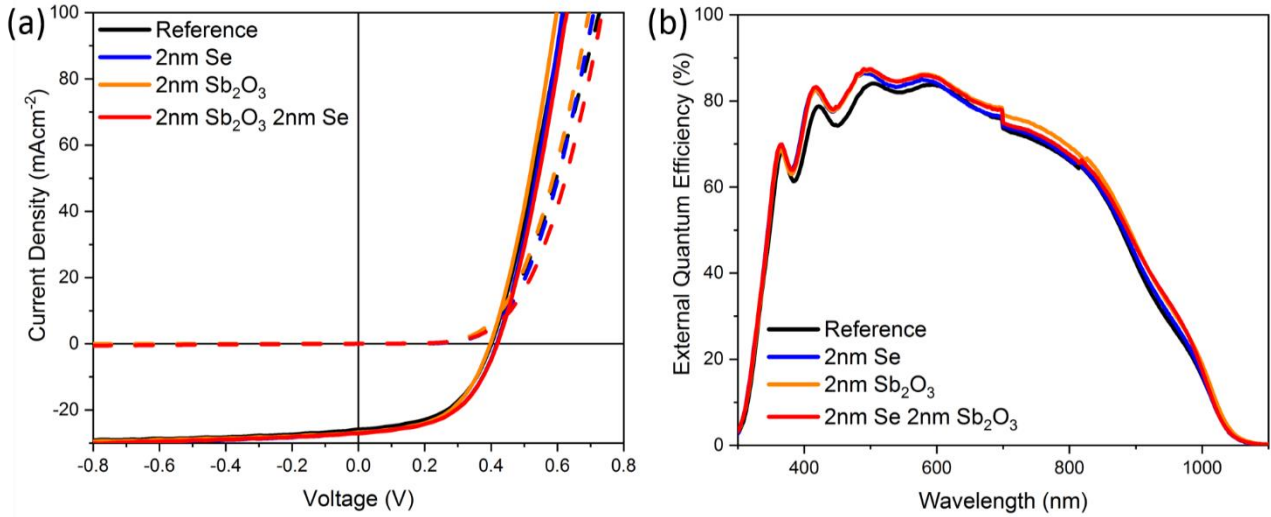
Figure 8: a) Current-voltage plots of a freshly made reference cell, and cells with 2 nm of thermally evaporated Sb_2O_3, Se, and both between the Sb_2Se_3 and Au layers, showing the reduction in roll-over and increase in J_{oc} and V_{oc}. b) External quantum efficiency.

the stoichiometry of evaporated films to be α-Sb_2O_3 [28, 29] and trigonal Se [30] (Fig. S11). A similar, although smaller decrease in roll-over is observed with the cells, analogous to air exposure (Fig. S12). This demonstrates that the improvement seen with air exposure is almost certainly caused by the oxidation of Sb_2Se_3, creating Sb_2O_3, a more Se-rich Sb_2Se_3 layer and some elemental Se as shown by XPS (Fig. 4 and 5). The EQE spectra (Fig. 8b), peaking at ~90%, show excellent collection at high energies due to low parasitic absorption from the wide-bandgap window layer of TiO_2. The long tail above ~800 nm is indicative of significant losses due to mid-gap states. The interference fringes are caused by internal reflections within the multi-layer structure, whereas the small discontinuities at 700 nm and 800 nm are artifacts due to diffraction-grating switching. The increase in current comes from a broad increase in the entire EQE (Fig. 8b), indicating increased collection throughout all wavelengths. Table 2 highlights that while thin layers of both Sb_2O_3 and Se increase device performance, the Se layer has a greater effect. This thin layer may react at the back surface to form a Se-rich Sb_2Se_3 film or remain on the surface. Further XPS analysis of thin deposited films might resolve this but is beyond the scope of this work. The thin layer of oxide improves J_{sc} by blocking shunting pathways and improving the

interface to the gold back contact. Overall, the combination of both materials is expected to yield the best device performance.

Thicker layers of Se and Sb_2O_3 were also investigated. Fig. S12 shows that the addition of 3 nm of Sb_2O_3 between the Sb_2Se_3 and Au layers in a device yields similar performance to reference devices, and 6 nm of Sb_2O_3 has a deleterious effect on the performance due to an increased series resistance. The addition of 5 nm of Se is also shown which demonstrated no improvement in device properties. This confirms that while a thin layer of Sb_2O_3 and Se has a positive effect, the lower conductivity of these layers puts a limit on the thickness that is beneficial to devices without further processing (diffusing the Se into the layer, for example).

Conclusions

In this study, we have shown that exposure to air increases the efficiency of n-type Sb_2Se_3 solar cells via a reduction in the back contact barrier height. This change occurs over a matter of days at room temperature and pressure, without any additional processing. Examination of the Sb_2Se_3 back surface using XPS revealed that over a 5-day period exposed to air, the amount of Sb_2O_3 present increased by 34% while the amount of free

Table 2: Peak and average (of 24 cells) η, V_{oc}, J_{sc} and FF for freshly made reference cells, and cells with 2 nm of thermally evaporated Sb_2O_3, Se, or both between the Sb_2Se_3 and Au layers.

	Peak				Average			
	η	V_{oc}	J_{sc}	FF	η	V_{oc}	J_{sc}	FF
Reference	**5.36**	0.401	25.84	51.90	**4.78**	0.396	25.69	46.91
2 nm Se	**5.85**	0.417	26.91	51.80	**5.41**	0.418	26.12	49.58
2 nm Sb_2O_3	**5.57**	0.398	26.71	52.10	**4.95**	0.393	26.25	47.94
2 nm Sb_2O_3 + 2 nm Se	**5.87**	0.419	27.02	51.70	**4.98**	0.393	25.95	48.10

selenium increased by 4%, leading to a more Se-rich Sb_2Se_3 layer forming at the back surface. The oxide species was analysed by Raman spectroscopy and found to be α-Sb_2O_3 (senarmonite). Exposure to 5 days of vacuum resulted in a loss of Se from the Sb_2Se_3 film, suggesting that the XPS measurements may underestimate selenium to antimony ratios in the sample. The presence of both antimony oxide and selenium enhance the back contact by improving change extraction and suppressing recombination. Therefore, the presence of a small amount of either of these materials reduces the back contact barrier height, as measured by *J-V-T*, from 320 meV to 280 meV thereby reducing the roll-over observed in *J-V* measurements and increasing the fill factor. This yields a relative efficiency improvement of the cells of *ca.* 10%. Selenium loss under vacuum increases the barrier height to 370 meV, with a corresponding loss in efficiency. Replicating these results by depositing thin layers of Sb_2O_3 and Se by thermal evaporation demonstrated that the most significant factor in enhancing the performance arises from excess selenium. Also, while 2 nm of oxide is beneficial, any more than this was detrimental to performance due to an increased series resistance. In this work a peak efficiency of 5.9% was achieved, without the use of organic charge transfer layers which often yield higher efficiency values. [13] These organic interlayers were omitted in this work to simplify confounding factors. These results demonstrate the importance of a more selenium rich back surface for high efficiency devices and the positive effects of a thin antimony oxide layer, explaining the possible function of back contact etching, and pointing a way forward for higher-efficiency devices.

Associated Content

Supporting Information

The supporting information is available free of charge at *INSERT DOI*

Transmittance spectra for cells after various periods of air exposure; Device performance of individual cells in a set after air exposure; Device performance after 120 hrs under vacuum; Sample fits to *J-V-T* data; Grazing incidence XRD of air exposed Sb_2Se_3; Raman spectra of air exposed and annealed samples; IMFP values calculated for different orbitals measured with XPS; SEC plots for samples exposed to different environments; Further details on WF analysis; Description and plots for band diagram generation; J-V of air annealed sample; Raman of thermal Sb_2O_3 and Se layers; XPS peak area comparison; XPS Se/Sb ratios; J-V curves of cells with thicker Sb_2O_3 and Se layers deposited.

Author Information

Corresponding Author

Laurie J. Phillips - *Stephenson Institute for Renewable Energy and Department of Physics, Peach Street, University of Liverpool, Liverpool L69 7ZF, UK*; E-mail: Laurie.Phillips@liverpool.ac.uk

Authors

Nicole Fleck - *Stephenson Institute for Renewable Energy and Department of Physics, Peach Street, University of Liverpool, Liverpool L69 7ZF, UK*

Oliver S. Hutter - *Department of Mathematics, Physics and Electrical Engineering, Northumbria University, Newcastle upon Tyne NE1 8ST, UK*

Huw Shiel - *Stephenson Institute for Renewable Energy and Department of Physics, Peach Street, University of Liverpool, Liverpool L69 7ZF, UK*

Theodore D. C. Hobson - *Stephenson Institute for Renewable Energy and Department of Physics, Peach Street, University of Liverpool, Liverpool L69 7ZF, UK*

Vin R. Dhanak - *Stephenson Institute for Renewable Energy and Department of Physics, Peach Street, University of Liverpool, Liverpool L69 7ZF, UK*

Tim D. Veal - *Stephenson Institute for Renewable Energy and Department of Physics, Peach Street, University of Liverpool, Liverpool L69 7ZF, UK*

Frank Jäckel - *Stephenson Institute for Renewable Energy and Department of Physics, Peach Street, University of Liverpool, Liverpool L69 7ZF, UK*

Ken Durose - *Stephenson Institute for Renewable Energy and Department of Physics, Peach Street, University of Liverpool, Liverpool L69 7ZF, UK*

Jonathan D. Major - *Stephenson Institute for Renewable Energy and Department of Physics, Peach Street, University of Liverpool, Liverpool L69 7ZF, UK*

Author contributions

‡ Nicole Fleck, Oliver S. Hutter and Laurie J. Phillips contributed equally to this work.

Notes

The authors declare no competing financial interest.

Acknowledgements

References

[1] Liu, X.; Chen, J.; Luo, M.; Leng, M.; Xia, Z.; Zhou, Y.; Qin, S.; Xue, D. J.; Lv, L.; Huang, H.; Niu, D.; Tang, J. Thermal Evaporation and Characterization of Sb_2Se_3 Thin Film for Substrate Sb_2Se_3/CdS Solar Cells. *ACS Appl. Mater. Interfaces*, 2014, **6**, 10687-10695.

[2] Li, Z.; Liang, X.; Li, G.; Liu, H.; Zhang, H.; Guo, J.; Chen, J.; Shen, K.; San, X.; Yu, W.; Schropp, R. E. I.; Mai, Y. 9.2%-Efficient Core-Shell Structured Antimony Selenide Nanorod Array Solar Cells. Nat. Commun., 2019, **10**, 125.

[3] Hobson, T. D. C.; Phillips, L. J.; Hutter, O. S.; Shiel, H.; Swallow, J. E. N.; Savory, C. N.; Nayak, P. K.; Mariotti, S.; Das, B.; Bowen, L.; Jones, L. A. H.; Featherstone, T. J.; Smiles, M. J.; Farnworth, M. A.; Zoppi, G.; Thakur, P. K.; Lee, T.; Snaith, H. J.; Leighton, C.; Scanlon, D. O.; Dhanak, V. R.; Durose, K.; Veal, T. D.; Major, J. D. Isotype Heterojunction Solar Cells using n-type Sb$_2$Se$_3$ Thin Films. Chem. Mater., 2020, **32**, 2621-2630.

[4] Williams, R. E.; Ramasse, Q. M.; McKenna, K. P.; Phillips, L. J.; Yates, P. J.; Hutter, O. S.; Durose, K.; Major, J. D.; Mendis, B. G. Evidence for Self-Healing Benign Grain Boundaries and a Highly Defective Sb$_2$Se$_3$-CdS Interfacial Layer in Sb$_2$Se$_3$ Thin-film Photovoltaics. ACS Appl. Mater. Inter., 2020, **12**, 21730-21738.

[5] Fleck, N.; Hobson, T. D. C.; Savory, C. N.; Buckeridge, J.; Veal, T. D.; Correia, M. R.; Scanlon, D. O.; Durose, K.; Jäckel, F. Identifying Raman Modes of Sb$_2$Se$_3$ and their Symmetries using Angle-resolved Polarised Raman Spectra. *J. Mater. Chem. A,* 2020, **8,** 8337-8344.

[6] Meng, L.; You, J.; Yang, Y. Addressing the Stability Issue of Perovskite Solar Cells for Commercial Applications. *Nat Commun.,* 2018, **9,** 5265.

[7] Jordan, D. C. and Kurtz, S. R. Photovoltaic Degradation Rates - an Analytical Review. *Prog. Photovoltaics Res. Appl.*, 2013, **21,** 12–29.

[8] Shiel, H.; Hutter, O. S.; Phillips, L. J.; Turkestani, M. A.; Dhanak, V. R.; Veal, T. D.; Durose, K.; Major, J. D. Chemical Etching of Sb$_2$Se$_3$ Solar Cells: Surface Chemistry and Back Contact Behaviour. *J. Phys. Energy,* 2019, **1**, 045001.

[9] Chen, C.; Zhao, Y.; Lu, S.; Li, K.; Li, Y.; Yang, B.; Chen, W.; Wang, L.; Li, D.; Deng, H.; Yi, F.; Tang, J. Accelerated Optimization of TiO$_2$/Sb$_2$Se$_3$ Thin Film Solar Cells by High-throughput Combinatorial Approach. *Adv. Energy Mater.,* 2017, **7,** 1700866.

[10] Tang, R.; Zheng, Z.; Su, Z.; Li, X.; Wei, Y.; Zhang, X.; Fu, Y.; Luo, J.; Fan, P.; Liang, G. Highly Efficient and Stable Planar Heterojunction Solar Cell Based on Sputtered and Post-Selenized Sb$_2$Se$_3$ Thin Film. *Nano Energy*, 2019, **64**, 103929.

[11] Leng, M.; Luo, M.; Chen, C.; Qin, S.; Chen, J.; Zhong, J.; Tang, J. Selenization of Sb$_2$Se$_3$ Absorber Layer: An Efficient Step to Improve Device Performance of CdS/Sb$_2$Se$_3$ Solar Cells. *Appl. Phys. Lett.*, 2014, **105**, 083905.

[12] Kumar, V.; Artegiani, E.; Kumar, A.; Mariotto, G.; Piccinelli, F.; Romeo, A. Effects of Post-deposition Annealing and Copper Inclusion in Superstrate Sb$_2$Se$_3$ Based Solar Cells by Thermal Evaporation. *Sol. Energy,* 2019, **193**, 452–457.

[13] Hutter, O. S.; Phillips, L. J.; Durose, K.; Major, J. D. 6.6% Efficient Antimony Selenide Solar Cells using Grain Structure Control and an Organic Contact Layer. *Sol. Energy Mater. Sol. Cells.*, 2018, **188,** 177–181.

[14] Phillips, L. J.; Savory, C. N.; Hutter, O. S.; Yates, P. J.; Shiel, H.; Mariotti, S.; Bowen, L.; Birkett, M.; Durose, K.; Scanlon, D. O.; Major, J. D. Current Enhancement via a TiO$_2$ Window Layer for CSS Sb$_2$Se$_3$ Solar Cells: Performance Limits and High V$_{oc}$. *IEEE J. Photovolt.,* 2019, **9,** 544-551.

[15] Mariotti, S.; Hutter, O. S.; Phillips, L. J.; Yates, P. J.; Kundu, B.; Durose, K. Stability and Performance of CsPbI$_2$Br Thin Films and Solar Cell Devices. *ACS Appl. Mater. Inter.,* 2018, **10,** 3750-3760.

[16] Bätzner, D. L.; Öszan, M. E.; Bonnet, D.; Bücher, K. Device Analysis Methods for Physical Cell Parameters of CdTe/Cds Solar Cells. *Thin Solid Films,* 2000, **361,** 288–292.

[17] Jain, V.; Biesinger, M. C.; Linford, M. R. The Gaussian-Lorentzian Sum, Product; Convolution (Voigt) Functions in the Context of Peak Fitting X-ray Photoelectron Spectroscopy (XPS) Narrow Scans. *Appl. Surf. Sci.,* 2018, **447**, 548-553.

[18] Shirley, D. A. High-resolution X-ray Photoemission Spectrum of the Valence Bands of Gold, *Physical Review B*, vol. 5, no. 12, p. 4709, 1972.

[19] Mavlonov, A.; Razykov, T.; Raziq, F.; Gan, J.; Chantana, J.; Kawano, Y.; Nishimura, T.; Wei, H.; Zakutayev, A.; Minemoto, T.; Zu, X.; Li, S.; Qiao, L. A Review of Sb$_2$Se$_3$ Photovoltaic Absorber Materials and Thin-Film Solar Cells. *Sol. Energy,* 2020, **201,** 227–246.

[20] Major, J. D.; Phillips, L. J.; Al Turkestani, M.; Bowen, L.; Whittles, T. J.; Dhanak, V. R.; Durose, K. P3HT as a Pinhole Blocking Back Contact for CdTe Thin Film Solar Cells, *Sol. Energy Mater. Sol. Cells,* 2017, **172,** 1–10.

[21] Demtsu, S.H.; Sites, J.R. Effect of Back-Contact Barrier on Thin-Film CdTe Solar Cells. *Thin Solid Films*, 2006, **510,** 320-324

[22] Neves, B. R. A.; Vilela, J. M. C.; Russell, P. E.; Reis, A. C. C.; Andrade, M. S. Imaging Micro-Cracks in Gold Films: A Comparative Study of Scanning Tunneling and Atomic Force Microscopies. *Ultramicroscopy,* 1999, **76,** 61–67.

[23] Stockman, L.; Vloeberghs, H.; Heyvaert, I.; Van Haesendonck, C.; Brynseraede, Y. Topographic Study of Thin Gold Films Grown on SiO$_2$. *Ultramicroscopy,* 1992, **42,** 1317–1320.

[24] Yeh, L. and Lindau, I. Atomic Subshell Photoionization Cross Sections and Asymmetry Parameters: 1 ≤ Z ≤ 103. *At. Data Nucl. Data Tables*, 1985, **32,** 1-155.

[25] Helander, M. G.; Greiner, M. T.; Wang, Z. B.; Lu, Z. H. Pitfalls in Measuring Work Function using Photoelectron Spectroscopy. *Appl. Surf. Sci.,* 2010, **256,** 2602–2605.

[26] Chen, C.; Wang, L.; Gao, L.; Nam, D.; Li, D.; Li, K.; Zhao, Y.; Ge, C.; Cheong, H.; Liu, H.; Song, H.; Tang, J. 6.5% Certified Efficiency Sb$_2$Se$_3$ Solar Cells using PbS Colloidal Quantum Dot Film as Hole-transporting Layer. *ACS Energy Lett*. 2017, **2,** 2125–2132.

[27] Greenwood, N. N.; Earnshaw, A. *Chemistry of the Elements*, p. 668. Oxford: Butterworth-Heinemann, second ed., 1997.

[28] Pereira, A.; Gracia, L.; Santamaría-Pérez, D.; Vilaplana, R.; Manjón, F.; Errandonea, D.; Nalin, M.; Beltrán, A. Structural and Vibrational Study of Cubic Sb$_2$O$_3$ under High Pressure. *Phys. Rev. B,* 2012, **85,** 174108.

[29] Mestl, G.; Ruiz, P.; Delmon, B.; Knozinger, H. Sb$_2$O$_3$/Sb$_2$O$_4$ in Reducing/ Oxidizing Environments: An In Situ Raman Spectroscopy Study. *J. Phys. Chem.,* 1994, **98,** 11276–11282.

[30] Nagata, K.; Ishibashi, K.; Miyamoto, Y. Raman and Infrared Spectra of Rhombohedral Selenium. *JPN J. Appl. Phys.,* 1981, **20,** 463–469.

Table of Contents Figure: